



Article

# Design and Implementation of a Printed Circuit Model for a Wideband Circularly Polarized Bow-Tie Antenna

Matthew J. Dodd \*  and Atef Z. Elsherbeni 

Department of Electrical Engineering, Colorado School of Mines, Golden, CO 80401, USA; aelsherb@mines.edu  
\* Correspondence: mdodd@mines.edu

**Abstract:** A crossed bow-tie antenna design for S- and C-Band (2.44–7.62 GHz) with a peak gain of 7.29 dBi is presented to achieve wideband radiation efficiency greater than 90% and circular polarization with a single feed point. The polarization of the antenna is modeled by the input admittance of crossed bow-ties, and the model predictions are validated by experiments. A wideband matching network is designed to be tightly integrated with the antenna and produce a 103% impedance bandwidth. The matching network is decomposed into an equivalent circuit model, and an analysis is presented to demonstrate the principles of the matching network design. A prototype of the optimized antenna design is fabricated and measured to validate the analysis.

**Keywords:** ultra-wideband antennas; dipole antennas; satellite antennas; impedance matching

## 1. Introduction

With the ongoing miniaturization of electronic components, the capabilities of compact wireless communication systems are increasing. In the realm of small, uncrewed aircraft and satellites, a low size, weight, power, and cost (SWaP-C) vehicle is capable of increasingly ambitious missions. Furthermore, the supporting electronics for software-defined radio systems (SDRs) are easily integrated into a CubeSat SWaP-C package in modern systems [1]. These radio systems enable a wide range of applications including high-throughput data links [2,3], precision navigation and timing [4], and earth remote sensing [5] using commercial off-the-shelf (COTS) components, thus reducing the time and cost typically associated with custom radio frequency front ends. The listed applications are leveraging the wide instantaneous bandwidth, adjustable frequency tuning, and flexible processing that SDR architectures provide.

Software-reconfigurable front ends require multi-functional antennas in the same low-SWaP-C character of CubeSat platforms. A variety of solutions for low-volume antennas that meet these requirements have been developed [6,7], which are adapting canonical antenna designs to be compatible with low-SWaP-C platforms. Some of the broadband antenna designs being adapted include spiral antennas [8,9], tightly coupled dipole arrays [10–13], and bow-tie antennas [14–20].

The bow-tie antenna has advantageous characteristics of a very wide operating bandwidth, consistent radiation patterns, and a planar low-profile form factor that does not require deployment mechanisms. Circular polarization is also critical for satellite-based systems due to the unpredictable orientation of the antenna. It is common to implement orthogonal linearly polarized antennas fed in quadrature to synthesize circular polarization [14,16]. However, this requires hybrid couplers or separate transceivers for each polarization, which inevitably increases the size and complexity of the design. In [21], we introduced a design to achieve circular polarization with a single feed, and in [22], we improved the bandwidth with an integrated matching network. Here, we expand those works with theoretical background forming the basis for the circular polarization, and far-field radiation measurements. The detailed design, matching network–equivalent circuit



**Citation:** Dodd, M.J.; Elsherbeni, A.Z. Design and Implementation of a Printed Circuit Model for a Wideband Circularly Polarized Bow-Tie Antenna. *Electronics* **2024**, *13*, 3323. <https://doi.org/10.3390/electronics13163323>

Academic Editor: Alejandro Melcón Alvarez

Received: 11 July 2024

Revised: 14 August 2024

Accepted: 19 August 2024

Published: 21 August 2024



**Copyright:** © 2024 by the authors. Licensee MDPI, Basel, Switzerland. This article is an open access article distributed under the terms and conditions of the Creative Commons Attribution (CC BY) license (<https://creativecommons.org/licenses/by/4.0/>).

analysis, and optimization process are also presented here. The primary contributions of this work are the following:

1. A design for a circularly polarized, wideband 2.44–7.62 GHz S- and C-Band antenna that does not require hybrid couplers or multiple feeds;
2. Analytical solutions to the input admittance of the antenna that can be used to adapt the design without time-consuming full-wave simulations and optimization;
3. An integrated matching network design to improve the bandwidth of the antenna;
4. An equivalent circuit model of the proposed matching network that can expedite the design of similar matching networks prior to full-wave simulation.

The remainder of this paper is organized as follows: Section 2 describes the theoretical basis for the antenna and matching network design, as well as methods used for optimizing the design. Section 3 contains results from a fabricated prototype of the optimized design, used to evaluate the validity of the models developed in Section 2. In Section 4, conclusions are drawn from the design and experiments.

## 2. Materials and Methods

The bow-tie antenna is a realization of the conical dipole antenna. An infinite model of the dipole may be analyzed as a tapered waveguide that supports infinite modes and is thus frequency-independent [23]. However, in finite realizations such as the bow-tie antenna, reflections from the termination of the dipole arms disrupt the fundamental mode and excite higher-order modes. These higher-order modes have an undesirable radiation pattern and higher radiation resistance, and thus limit the efficiency and bandwidth.

### 2.1. Polarization Mechanism

The analytical model of the finite tapered dipole presented in [23,24] is a tapered transmission line terminated with a load equivalent to the radiation resistance. The transmission line's characteristic impedance is based on the taper angle,  $\alpha$ , as shown in Figure 1a.

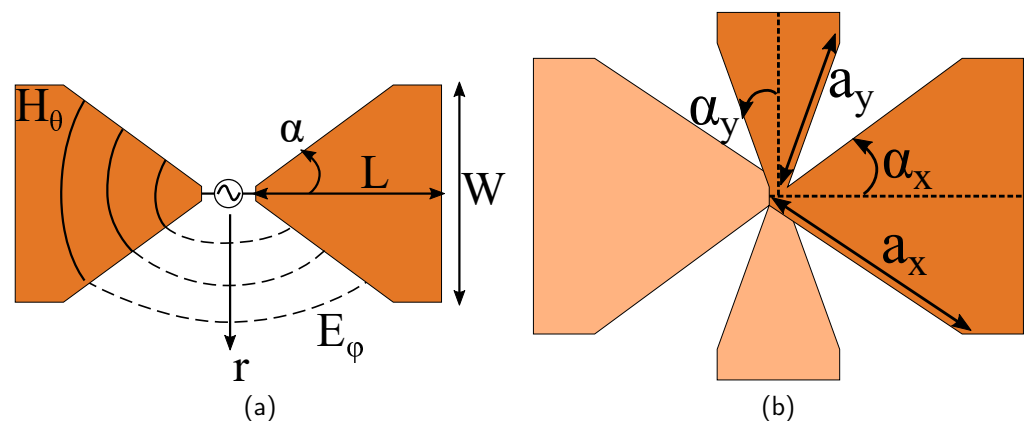


**Figure 1.** (a) TEM mode supported by the tapered transmission line formed in the bow-tie antenna. (b) Geometric parameters for analyzing the input impedance of the bow-tie antenna model. The darker shade of orange represents metallization on the top side of a dielectric substrate and the lighter shade represents metallization on the bottom side.

The input impedance of the tapered bow-tie can be computed analytically using the methods presented in [25]. To produce circularly polarized radiation, we implement two orthogonally oriented crossed bow-ties as shown in Figure 1b. The feed is connected to these bow-ties in parallel, so we will analyze their complex input admittances,  $Y_x$  and  $Y_y$ . Perfectly circular radiated fields occur when the vertical and horizontal electric field components are equal in magnitude but 90 degrees out of phase. In terms of input admittance,

$$G_x = G_y \quad (1)$$

$$\text{sign } B_x = -\text{sign } B_y \quad (2)$$

are the conditions for circularly polarized radiation from the crossed bow-ties, where  $G_x$  and  $G_y$  are the conductance, and  $B_x$  and  $B_y$  are the susceptance of the horizontal and vertical bow-ties, respectively.

There are two geometric parameters that control the input admittance of the dipoles. First is the flare length  $a$ , which is normalized to the wave number/propagation constant  $k = \frac{2\pi}{\lambda}$  and analyzed as the product  $ka$ . Second is the flare angle  $\alpha$ , which determines the characteristic impedance [25]:

$$Z_0 = 60 \ln \cot \frac{\alpha}{2}. \quad (3)$$

For an infinite bow-tie antenna, the input impedance is frequency-independent and equal to the characteristic impedance. However, the finite length of the bow-tie arms causes the input impedance to vary with frequency. The characteristic impedance is equal to the input impedance at the center frequency of the designed operating band,  $f_c$  (5 GHz in the design presented here). In Figure 2, the input impedance is calculated as a function of frequency normalized to the center frequency, i.e.,  $\frac{f}{f_c}$ . The optimized crossed bow-tie design presented in this paper has the parameters  $ka_x = 0.22$ ,  $ka_y = 0.19$ ,  $\alpha_x = 17.1^\circ$ , and  $\alpha_y = 12.0^\circ$ . These parameters give the basic dimensions of the bow-tie elements, as shown in Figure 1b. The radiation polarization characteristics are primarily determined by these dimensions. In the later sections, we will add a matching network to improve the impedance match to a 50 ohm coaxial line, but the radiating element dimensions will remain unchanged.

The results shown in Figure 2 suggest ideal circular polarization at  $0.77f_c$  and inversion of the rotational sense at  $1.1f_c$ . At the frequency where circular sense is switched, we expect a local maximum in  $S_{11}$ . These results will be confirmed by experimental data from the prototype antenna fabricated in this work.

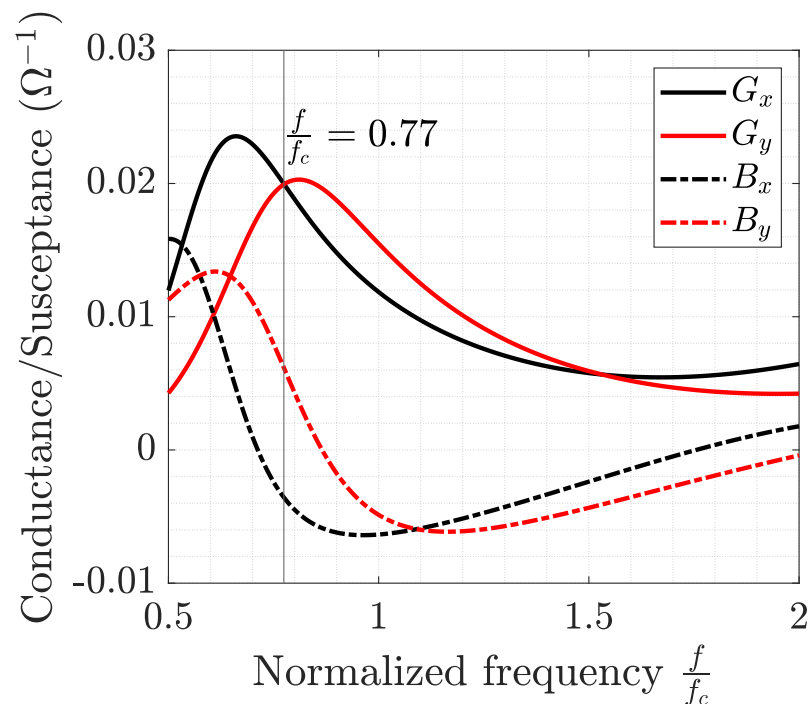


**Figure 2.** Input admittance of two crossed dipoles with  $ka_x = 0.22$ ,  $ka_y = 0.19$ ,  $\alpha_x = 17.1^\circ$ , and  $\alpha_y = 12.0^\circ$ .

## 2.2. Optimization

The first iteration of the antenna design did not have a matching network, as shown in Figure 1b. The simulated input impedance of this design showed that the antenna input was not well matched to a 50 Ohm coaxial feed line. This initial result set is shown as the ‘Antenna 1’ plot in Figure 3. To improve the impedance matching, a matching network was designed and added. The matching network consists of printed circuit elements to improve the ease of manufacturing and maintain the low cost of the antenna. The primary mismatch contribution is from the capacitance of the bow-tie arms; thus, the matching network is made of two pairs of printed loop inductors. An equivalent circuit model is shown in Figure 4 alongside the printed elements used to represent the lumped circuit elements.

There are three parameters shown in the Figure 4 matching network schematic to tune for impedance matching: inductor radius (R), capacitive gap (G), and transmission line length (L). To obtain uni-directional radiation, the bow-tie antenna is placed above a ground plane, which also affects the input impedance of the antenna. Therefore, we must include the air gap height as a parameter to be optimized with the matching network. To optimize the matching network for wideband operation, we use a cost function of the simulated  $S_{11}$ :

$$\text{cost} = \text{avg}(S_{11}) + \max(S_{11}). \quad (4)$$

The independent variable in (4) is the frequency evaluated by the solver. For this optimization, we used the FEM solver in Ansys HFSS 2024 R2 and evaluated 51 frequency points from 3–8 GHz. Test parameter sets for each iteration were produced using the HFSS Multi-Objective Genetic Algorithm, with the objective of minimizing the cost function (4). At the end of the optimization process, the impedance match is improved, as indicated by  $S_{11}$  being less than  $-10$  dB continuously from 2.25 to 8 GHz in the ‘Antenna 2’ plot in Figure 3. Additionally, the radiation efficiency is on average 0.935 and always greater than 0.9 across the band.

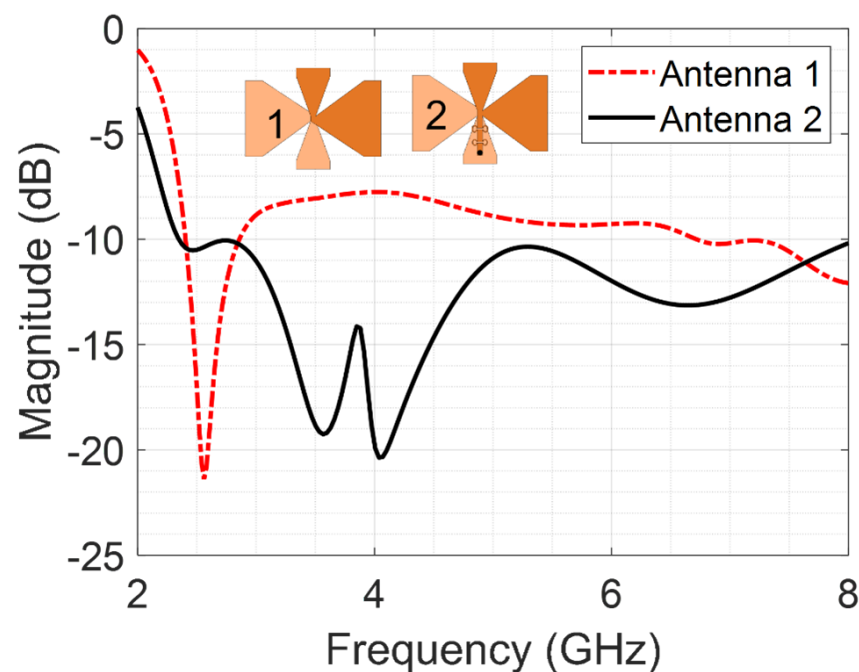


**Figure 3.** Simulated  $S_{11}$  results of initial design (antenna 1) compared to that of optimized design (antenna 2).

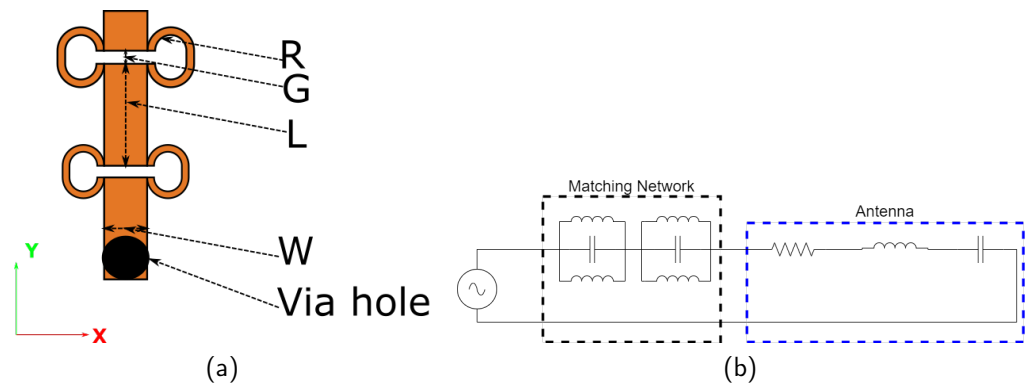


**Figure 4.** (a) The optimized matching network consists of an inductor radius ( $R$ ), a capacitor gap ( $G$ ), a transmission line length ( $L$ ), and a transmission line width ( $W$ ). (b) The equivalent circuit of the matching network.

An equivalent circuit model of the matching network and antenna is shown in Figure 4. To validate this model, we use an analytical calculation of the input impedance from simulated S-parameters of the unmatched antenna and lumped circuit elements. The calculation is performed using a subnetwork growth algorithm [26] implemented using scikit-rf v1.2.0 [27]. We aimed to extract lumped element values that approximate those of the printed circuit elements in the matching network. This is accomplished by calculating the input impedance of the equivalent circuit model and comparing it to the input impedance of the full wave simulation of the antenna with the matching network. The lumped element values are obtained using gradient descent optimization to minimize  $|Z_{eq} - Z_{fw}|$ , where  $Z_{eq}$  is the equivalent circuit input impedance,  $Z_{fw}$  is the full wave input impedance from HFSS, and  $|\cdot|$  is the 1-norm of the vector of impedance values at all sampled frequency points. A finite difference approximation of the gradient is used in the optimization.

The results of the equivalent circuit model extraction in Figure 5 show good agreement with the measured results above 4 GHz. With the longer wavelength at frequencies below 4 GHz, there is more interaction between the fields of the antenna elements and the fields of the printed circuit elements. In the equivalent circuit model, the antenna elements and circuit elements are modeled as lumped impedances, and any interactions between the fields are not evaluated. The divergence of the results below 4 GHz indicates that there is interaction between the fields of the antenna elements and matching network lumped elements, and the input impedance is affected in a way that is not modeled by the equivalent circuit model.

The extracted equivalent circuit parameters are 7.49 nH for the inductor loops and 66.43 fF for the capacitive gaps. The close agreement of these results indicate that this method of equivalent circuit modeling for this matching network design could be used to generate starting design parameters for full-wave simulation optimization that are closer to the optimal. This approach could reduce the optimization time for the full-wave simulation portion of the process.

After full-wave simulation optimization using HFSS, as previously described, the optimized dimensions produced are shown in Figure 6a. The surface current density of the optimized design is shown in Figure 7. The antenna is placed above a ground plane to produce a directional radiation pattern. Additionally, the ground plane separates the radiating elements of the antenna from the feeding network and other electronics. The simulated  $-10$  dB  $S_{11}$  bandwidth of this optimized design is from 2.25 GHz to 8 GHz, yielding  $f_c = 5.2$  GHz. From this, we determine the parameters used in the admittance calculation in Figure 2,  $ka_x = 0.22$  and  $ka_y = 0.19$ . A prototype antenna was fabricated using these dimensions, the analysis of which is presented in the following section.

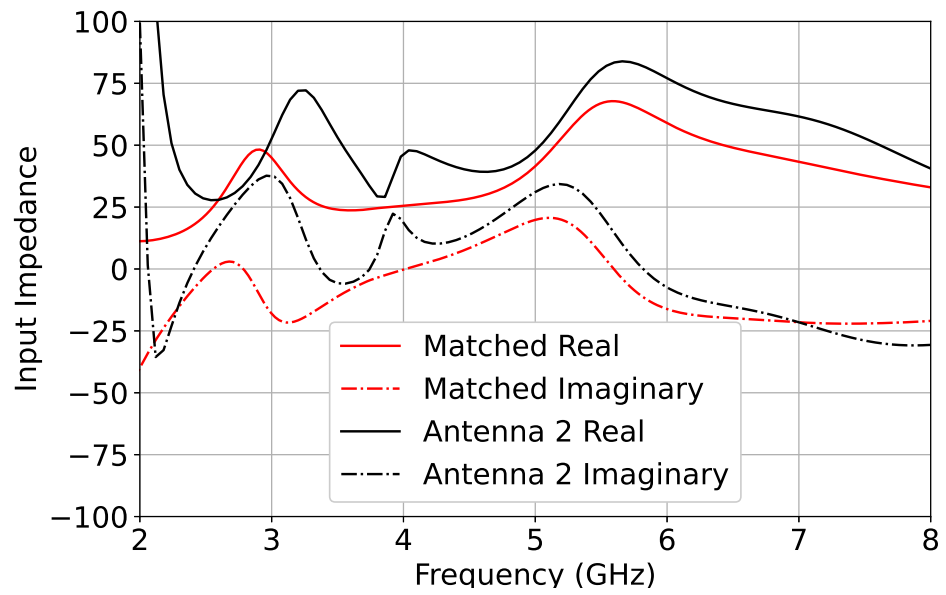


**Figure 5.** ‘Matched Real’ and ‘Matched Imaginary’ show the input impedance of the equivalent circuit model with extracted values to match the full wave simulations from HFSS, which are plotted as ‘Antenna 2 Real’ and ‘Antenna 2 Imaginary’.

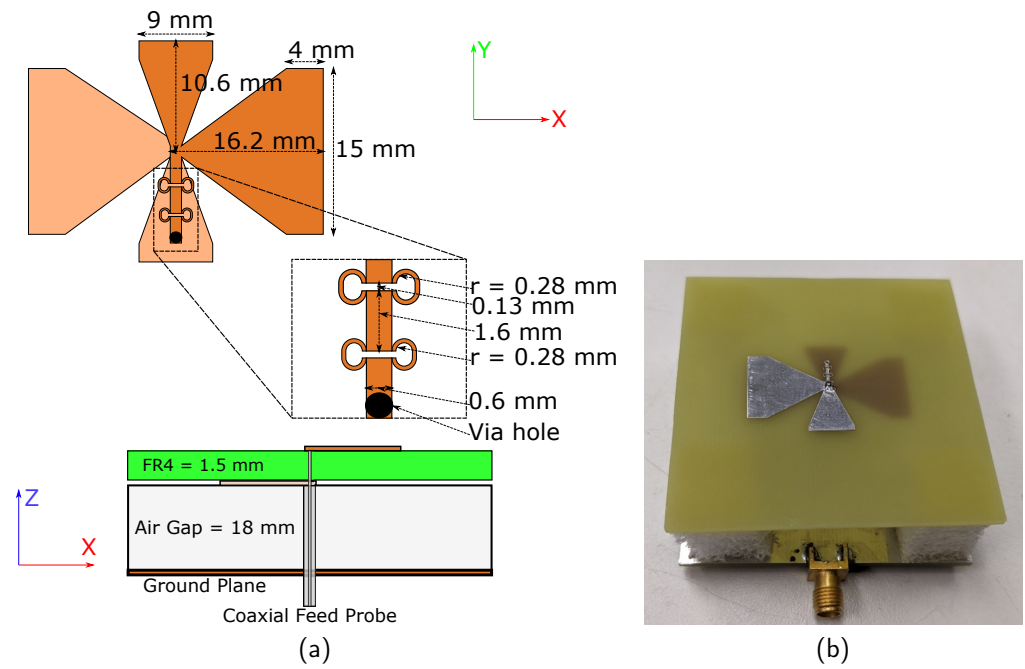


**Figure 6.** (a) Dimensions of the optimized antenna with matching network. (b) Photograph of the fabricated prototype antenna, including the antenna PCB, foam spacers, coaxial feed, and microstrip feed line to the SMA connector.



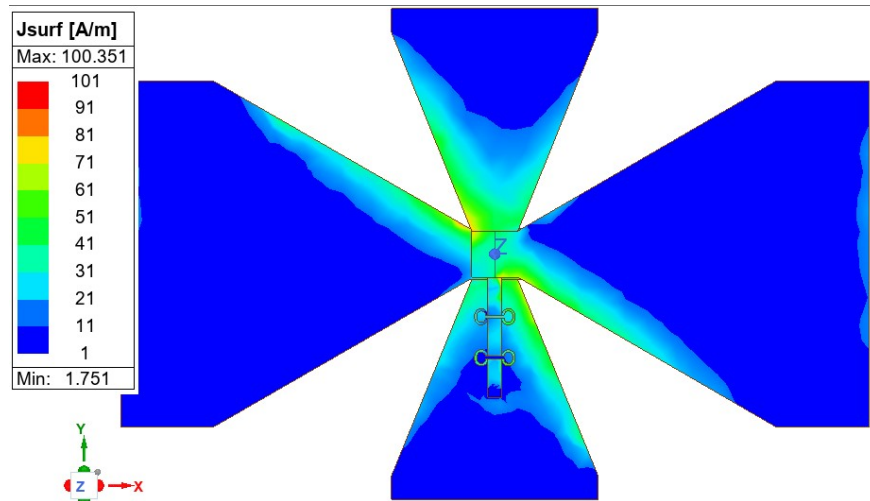


**Figure 7.** Surface current distribution at 5 GHz for the optimized antenna 2 design with a printed matching network.

### 3. Results and Discussion

A photograph of the fabricated antenna is shown in Figure 6a. The antenna and feeding microstrip to the SMA transition were printed on separate FR4 PCBs. The purpose of the microstrip feed board is to demonstrate a pathway to incorporating this antenna design into array configurations with an integrated feed network. The microstrip ground plane serves a dual purpose as the ground reflector for the antenna. In this prototype, the microstrip simply serves as a transition from the edge launch SMA connector to the semi-rigid coaxial cable. The inner conductor of the coaxial cable is soldered to the microstrip, and the outer conductor is soldered to the ground plane on the opposite side. On the antenna side, the inner conductor is attached to the top layer's bow-tie, arm and the outer conductor is attached to the bottom layer's bow-tie arm, as shown in Figure 6a. Both PCBs are fabricated using 1.5 mm thick substrate.

The  $S_{11}$  of the prototype antenna was measured with a Keysight FieldFox VNA from 2 GHz to 8 GHz and plotted against simulation results in Figure 8a. The results are in good agreement with the simulation and are less than  $-10$  dB from 2.44 GHz to 7.62 GHz for an impedance bandwidth of 103%. As predicted using the calculated admittances shown in Figure 2, there is a local maximum in the  $S_{11}$  curve slightly above  $f_c$ . The analytical admittance calculations shown in Figure 2 do not account for the effects of the matching network and only represent the admittance of the bow-tie elements.

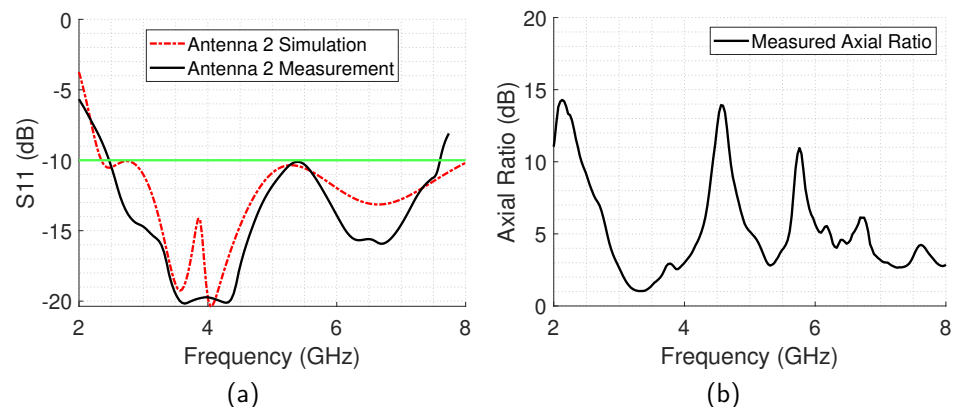


**Figure 8.** (a) The simulated and measured  $S_{11}$  of the optimized antenna design compared to the simulated  $S_{11}$  of antenna 1. The  $-10$  dB reference line for  $S_{11}$  is plotted in green. (b) The measured axial ratio of the prototype antenna.

The radiation patterns of the prototype were measured using the Colorado School of Mines anechoic chamber following the procedures described in [28]. The axial ratio is computed from the ratio of the semi-major and semi-minor axes of the polarization ellipse. Normalized radiation patterns collected at 3 GHz, 4 GHz, and 5 GHz are shown in Figure 9 and compared to the simulated radiation patterns. We observed good agreement between the simulated and measured patterns. The peak measured gain of the prototype antenna was 7.29 dBi. Additionally, the difference between two circular senses was larger for 3 GHz and 4 GHz compared to 5 GHz and is also confirmed in the axial ratio measurement shown in Figure 8b. This agrees with the predicted characteristics from the analytical calculation of the crossed bow-tie admittance: (1) better circular polarization at approximately  $0.77f_c$ , (2) relatively poor circular polarization at approximately  $1.1f_c$ , and (3) circular sense of the polarization is reversed above  $1.1f_c$ . The key results of the design proposed in this work are compared against similar designs in recently published literature in Table 1.

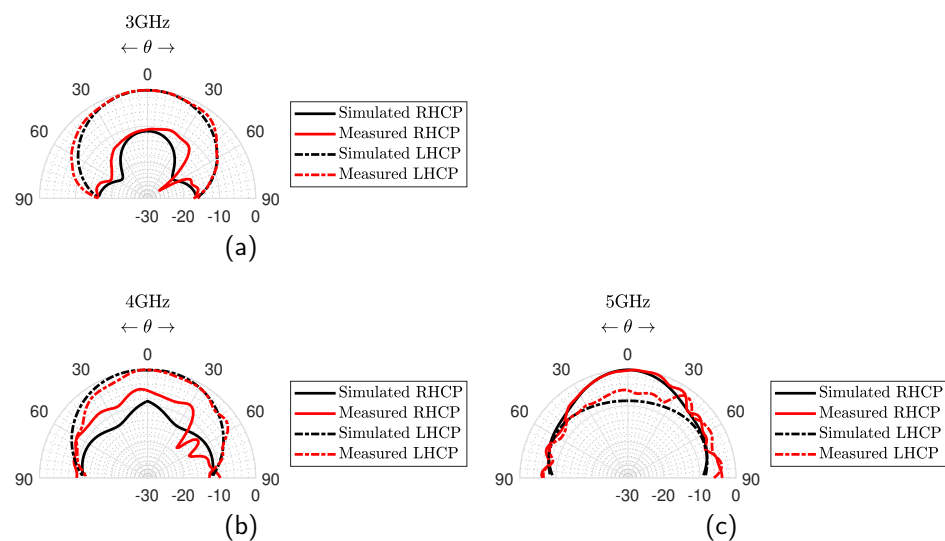


**Figure 9.** Measured and simulated normalized radiation patterns at (a) 3 GHz, (b) 4 GHz, and (c) 5 GHz.

**Table 1.** Key results of the proposed design compared with similar works.

Ref.	Freq. Range	Impedance BW	Polarization	Peak Gain
This Work	2.44–7.62 GHz	103%	Circular, one feed	7.29 dBi
[15]	3.1–5.0 GHz	47%	Dual, two feeds	7.5 dBi
[16]	2.21–6.06 GHz	93%	Circular, one feed	8.6 dBi
[17]	1.0–6.0 GHz	143%	Linear, balun feed	NA <sup>1</sup>
[18]	2.64–3.60 GHz	31%	Linear, balun feed	7.4 dBi
[19]	0.32–0.93 GHz	98%	Linear, single feed	9.3 dBi
[20]	0.25–0.85 GHz	109%	Linear, balun feed	4 dBi

<sup>1</sup> Peak gain not provided

#### 4. Conclusions

The crossed bow-tie antenna with 103% impedance bandwidth for S- and C-band (2.44–7.62 GHz) was presented, and prototype results are shown to confirm the effectiveness of the design approach. A peak measured gain of 7.29 dBi is achieved with an average radiation efficiency of 0.935 across the operating bandwidth. Analytical solutions to the bow-tie admittance are shown to be an effective method of predicting the antenna characteristics. In future adaptations, the admittance calculation could be used to optimize the design for a given application prior to full-wave electromagnetic simulations. The ratio between the lengths of the two crossed bow-ties, which were evaluated by admittance analysis, may be adjusted to control the circular polarization frequency characteristics.



Additionally, a matching network design and accompanying equivalent circuit model is presented, which effectively improves the impedance matching bandwidth of the designed antenna. The matching network is realized by printed inductors and a capacitor adjacent to the antenna structure, thus eliminating the need for external matching components. The equivalent circuit model provides a method to generate approximate values for the circuit elements required for matching prior to the final tuning of the geometry in full-wave simulation models.

**Author Contributions:** M.J.D. performed the antenna design, simulation, optimization, fabrication, and measurements, as well as prepared the manuscript. A.Z.E. directed the design, advised on measurement, and interpreted results, as well as reviewed and edited the manuscript. All authors have read and agreed to the published version of the manuscript.

**Funding:** The authors declare that this study received funding from Augustus Aerospace Company. The funder was not involved in the study design, collection, analysis, interpretation of data, the writing of this article, or the decision to submit it for publication.

**Data Availability Statement:** Data are contained within the article.

**Conflicts of Interest:** The authors declare no conflicts of interest.

## References

1. Theoharis, P.I.; Raad, R.; Tubbal, F.; Ali Khan, M.U.; Liu, S. Software-Defined Radios for CubeSat Applications: A Brief Review and Methodology. *IEEE J. Miniaturization Air Space Syst.* **2021**, *2*, 10–16. [[CrossRef](#)]
2. Devaraj, K.; Ligon, M.; Blossom, E.; Breu, J.; Klofas, B.; Colton, K.; Kingsbury, R.; Street, H.; Francisco, S. Planet High Speed Radio: Crossing Gbps from a 3U Cubesat. In Proceedings of the 2019 Small Satellite Conference Logan, UT, USA, 3–8 August 2019; p. 10.
3. Kaneko, T.; Kawano, N.; Nagao, Y.; Murakami, K.; Watanabe, H.; Mita, M.; Tomoda, T.; Hirako, K.; Shirasaka, S.; Nakasuka, S.; et al. 2.65Gbps Downlink Communications with Polarization Multiplexing in x-Band for Small Earth Observation Satellite. *IEICE Trans. Commun.* **2021**, *E104.B*, 1–12. [[CrossRef](#)]
4. Ellison, S.M.; Nanzer, J.A. High-Accuracy Multinode Ranging For Coherent Distributed Antenna Arrays. *IEEE Trans. Aerosp. Electron. Syst.* **2020**, *56*, 4056–4066. [[CrossRef](#)]
5. Peral, E.; Im, E.; Wye, L.; Lee, S.; Tanelli, S.; Rahmat-Samii, Y.; Horst, S.; Hoffman, J.; Yun, S.H.; Imken, T.; et al. Radar Technologies for Earth Remote Sensing From CubeSat Platforms. *Proc. IEEE* **2018**, *106*, 404–418. [[CrossRef](#)]
6. Rahmat-Samii, Y.; Manohar, V.; Kovitz, J.M. For Satellites, Think Small, Dream Big: A Review of Recent Antenna Developments for CubeSats. *IEEE Antennas Propag. Mag.* **2017**, *59*, 22–30. [[CrossRef](#)]
7. Gao, S.; Clark, K.; Unwin, M.; Zackrisson, J.; Shiroma, W.A.; Akagi, J.M.; Maynard, K.; Garner, P.; Boccia, L.; Amendola, G.; et al. Antennas for Modern Small Satellites. *IEEE Antennas Propag. Mag.* **2009**, *51*, 40–56. [[CrossRef](#)]
8. Dyson, J. The Equiangular Spiral Antenna. *IRE Trans. Antennas Propag.* **1959**, *7*, 181–187. [[CrossRef](#)]
9. Volakis, J.; Nurnberger, M.; Filipovic, D. Slot Spiral Antenna. *IEEE Antennas Propag. Mag.* **2001**, *43*, 15–26. [[CrossRef](#)]
10. Manohar, V.; Bhardwaj, S.; Venkatakrishnan, S.B.; Volakis, J.L. VHF/UHF Ultrawideband Tightly Coupled Dipole Array for CubeSats. *IEEE Open J. Antennas Propag.* **2021**, *2*, 702–708. [[CrossRef](#)]
11. Wheeler, H. Simple Relations Derived From a Phased-Array Antenna Made of an Infinite Current Sheet. *IEEE Trans. Antennas Propag.* **1965**, *13*, 506–514. [[CrossRef](#)]
12. Doane, J.P.; Sertel, K.; Volakis, J.L. A Wideband, Wide Scanning Tightly Coupled Dipole Array with Integrated Balun (TCDA-IB). *IEEE Trans. Antennas Propag.* **2013**, *61*, 4538–4548. [[CrossRef](#)]
13. Jordan, J.W.; Stacy, W.; Ng, J.; Cannon, B.L.; Caba, A.; Vanhille, K.J.; Clough, J.; Stant, B.; Racette, P.E. PolyStrata® X/Ku/K/Ka-band, Dual-Polarized, Tightly Coupled Dipole Scannable Focal Plane Array. In Proceedings of the 2018 IEEE International Symposium on Antennas and Propagation USNC/URSI National Radio Science Meeting, Boston, MA, USA, 8–13 July 2018; pp. 817–818. [[CrossRef](#)]
14. Eldek, A.; Elsherbeni, A.; Smith, C. Wide-Band Modified Printed Bow-Tie Antenna with Single and Dual Polarization for C- and X-band Applications. *IEEE Trans. Antennas Propag.* **2005**, *53*, 3067–3072. [[CrossRef](#)]
15. Alibakhshikenari, M.; Virdee, B.S.; See, C.H.; Shukla, P.; Mansouri Moghaddam, S.; Zaman, A.U.; Shafqaat, S.; Akinsolu, M.O.; Liu, B.; Yang, J.; et al. Dual-Polarized Highly Folded Bowtie Antenna with Slotted Self-Grounded Structure for Sub-6 GHz 5G Applications. *IEEE Trans. Antennas Propag.* **2022**, *70*, 3028–3033. [[CrossRef](#)]
16. Feng, G.; Chen, L.; Wang, X.; Xue, X.; Shi, X. Broadband Circularly Polarized Crossed Bowtie Dipole Antenna Loaded With Parasitic Elements. *IEEE Antennas Wirel. Propag. Lett.* **2018**, *17*, 114–117. [[CrossRef](#)]
17. Fiser, O.; Hruby, V.; Vrba, J.; Drizdal, T.; Tesarik, J.; Vrba, J., Jr.; Vrba, D. UWB Bowtie Antenna for Medical Microwave Imaging Applications. *IEEE Trans. Antennas Propag.* **2022**, *70*, 5357–5372. [[CrossRef](#)]
18. Jeong, J.; Park, K.; Lee, C. Design of Cavity-Backed Bow-Tie Antenna with Matching Layer for Human Body Application. *Sensors* **2019**, *19*, 4015. [[CrossRef](#)] [[PubMed](#)]

19. Pi, S.; Wang, T.; Lin, J. Directional and High-Gain Ultra-Wideband Bow-Tie Antenna for Ground-Penetrating Radar Applications. *Remote Sens.* **2023**, *15*, 3522. [[CrossRef](#)]
20. Yang, G.; Ye, S.; Ji, Y.; Zhang, X.; Fang, G. Radiation Enhancement of an Ultrawideband Unidirectional Folded Bowtie Antenna for GPR Applications. *IEEE Access* **2020**, *8*, 182218–182228. [[CrossRef](#)]
21. Dodd, M.J.; Elsherbeni, A.Z. A Wideband Circularly Polarized Printed Bow-Tie Antenna for Low-SWaP Aerial Applications. In Proceedings of the 2022 IEEE 20th Biennial Conference on Electromagnetic Field Computation (CEFC), Virtual, 24–26 October 2022; pp. 1–2. [[CrossRef](#)]
22. Dodd, M.J.; Elsherbeni, A.Z. Bowtie Antenna with Integrated Matching Network for Wideband and Circular Polarization. In Proceedings of the 2023 IEEE International Symposium on Antennas and Propagation and USNC-URSI Radio Science Meeting (USNC-URSI), Portland, OR, USA, 23–28 July 2023; pp. 1531–1532. [[CrossRef](#)]
23. Schelkunoff, S. *Electromagnetic Waves*; Bell Telephone Company Series; Van Nostrand: New York, NY, USA, 1943.
24. Balanis, C.A. *Antenna Theory: Analysis and Design*; Wiley: Hoboken, NJ, USA, 2005.
25. Papas, C.; King, R. Input Impedance of Wide-Angle Conical Antennas Fed by a Coaxial Line. *Proc. IRE* **1949**, *37*, 1269–1271. [[CrossRef](#)]
26. Compton, R. Perspectives in Microwave Circuit Analysis. In Proceedings of the 32nd Midwest Symposium on Circuits and Systems, Champaign, IL, USA, 14–16 August 1989; Volume 2, pp. 716–718. [[CrossRef](#)]
27. Arsenovic, A.; Hillairet, J.; Anderson, J.; Forstén, H.; Rieß, V.; Eller, M.; Sauber, N.; Weikle, R.; Barnhart, W.; Forstmayr, F. Scikit-Rf: An Open Source Python Package for Microwave Network Creation, Analysis, and Calibration [Speaker’s Corner]. *IEEE Microw. Mag.* **2022**, *23*, 98–105. [[CrossRef](#)]
28. *IEEE Std 149-2021 (Revision of IEEE Std 149-1977)*; IEEE Recommended Practice for Antenna Measurements. IEEE: Piscataway, NJ, USA, 2022; pp. 1–207. [[CrossRef](#)]

**Disclaimer/Publisher’s Note:** The statements, opinions and data contained in all publications are solely those of the individual author(s) and contributor(s) and not of MDPI and/or the editor(s). MDPI and/or the editor(s) disclaim responsibility for any injury to people or property resulting from any ideas, methods, instructions or products referred to in the content.